

SCIENTIFIC REPORTS

OPEN

Nonvolatile and ultra-low-loss reconfigurable mode (De) multiplexer/switch using triple-waveguide coupler with $\text{Ge}_2\text{Sb}_2\text{Se}_4\text{Te}_1$ phase change material

Weifeng Jiang 

Mode-division multiplexing (MDM) is a promising approach to dramatically enhance the transmission capacity. A reconfigurable mode (De)multiplexer/switch (RMDS) is a key component for the flexible mode routing in the MDM network. A nonvolatile and ultra-low-loss RMDS is proposed via a triple-silicon-waveguide directional coupler with the $\text{Ge}_2\text{Sb}_2\text{Se}_4\text{Te}_1$ (GSST) phase change material (PCM). The nonvolatile property of GSST makes it attractive to reduce the switching power-consumption. Benefiting from the low loss of the GSST-PCM at both amorphous and crystalline states, an RMDS with an ultra-low loss and a high extinction-ratio can be realized. The proposed RMDS is optimally designed by using the full-vectorial finite element method and 3D full-vectorial finite difference time domain method. The numerically simulated results show that a compact RMDS is with the extinction ratios of 18.98 dB and 22.18 dB, ultra-low insertion losses of 0.10 dB and 0.68 dB for the "OFF" and "ON" states, respectively at the operating wavelength of 1550 nm. An ultra-wide bandwidth of 100 nm is achieved for both the "OFF" and "ON" states.

Mode-division multiplexing (MDM) has been attracted much attention as a promising approach for dramatically enhancing the transmission capacity^{1,2}. MDM offers a new dimension for the optical network by exploiting orthogonal spatial modes as multiple signal channels for each operating wavelength, which can further significantly increase the spectral efficiency. To build a MDM network on-chip, many key components have been reported, including the mode multiplexers (MUXs)/demultiplexers (DeMUXs)³, mode filters⁴, mode converters⁵, two-mode power splitter⁶, mode switches⁷ and so on. Among them, the reconfigurable mode (De)MUX/switch (RMDS) is a basic and indispensable block for a reconfigurable and flexible MDM network, which can switch and route data signals in the multimode channels. However, the RMDS for a MDM network is more complex and requires new mechanisms to achieve the mode switchable functionality, compared with the conventional single-mode (SM) optical switches in the wavelength-division multiplexing (WDM) networks⁸.

Only a few RMDSes have been reported based on the Mach–Zehnder interferometers (MZIs)⁹, micro-ring resonators¹⁰, and multimode interference (MMI) structures with phase shifters¹¹. One approach could be the use of the MZIs with phase shifters. A 2×2 multimode optical switch was experimentally achieved with a link-crosstalk for all four modes of < -18.8 dB, composed of two mode DeMUXs, $n \times 2$ SM optical switches and two mode MUXs⁹. This reported approach is based on the independent processing of the single modes' signals using SM switches, in which the input multimode signals are firstly all converted into the fundamental mode (mode-conversion process); and then, the optical signals are switched by processing of individual channels using conventional optical switches (mode-switching process); finally, the SM signals are reconverted into their original higher-order modes at the output ports (mode-reconversion process). Although this approach can provide

College of Electronic and Optical Engineering, Nanjing University of Posts and Telecommunications, Nanjing, 210023, China. Correspondence and requests for materials should be addressed to W.J. (email: jwf@njupt.edu.cn)

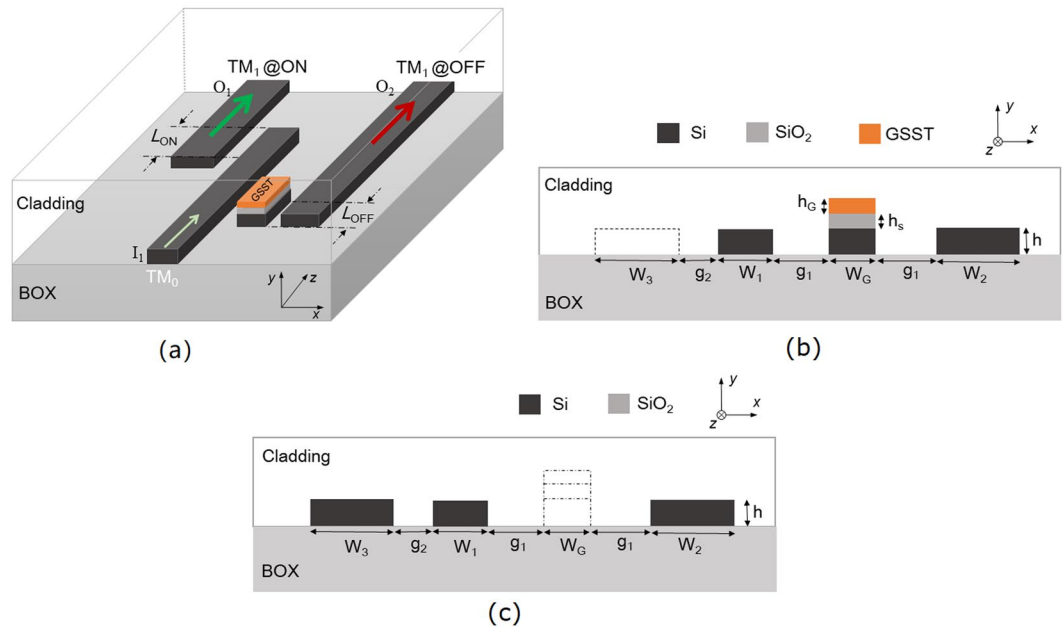


Figure 1. Nonvolatile reconfigurable mode (De)MUX/switch (RMDS). **(a)** Schematic of the proposed RMDS; **(b,c)** are cross-sections of the triple- and two-WG DCs over the lengths of L_{OFF} and L_{ON} , respectively.

a mode switch with a high-performance, this structure would also need extra mode-converters and a large footprint. Another approach could be the use of the micro-ring resonators based structures. B. Stern *et al.* have proposed and demonstrated an on-chip MDM switch based on the micro-rings, which routes four data channels with a low crosstalk (CT) of < -16.8 dB¹⁰. However, this reported approach is also based on the mode-conversion and mode-reconversion mechanism. In addition, the operating bandwidth and thermal stability of the MDM switch are limited by the micro-ring resonators. Another approach could be the use of the combination of the MMI, Y-branches, and phase shifters. A high-speed two-mode switch has been demonstrated by using this approach, which can achieve a measured switching extinction ratio (ER) of 12.5 dB¹¹. However, due to the weak nonlinear electro-optic (EO) effect of silicon material, the footprint of the reported mode-switch is as large as $0.3 \text{ mm} \times 0.6 \text{ mm}$. In order to achieve a compact RMDS with the high performance, the light-matter-interaction needs to be improved inside the device by introducing new structures and mechanisms.

Recently, optical phase change materials (PCMs) based SM optical switches have emerged for on-chip signals switching and routing, including indium tin oxide (ITO), graphene, vanadium dioxide (VO_2) and $\text{Ge}_2\text{Sb}_2\text{Te}_5$ (GST)^{12–15}. The high light-matter-interactions and compact footprints can be achieved benefiting from giant index-change (>1) of these PCMs. However, two mostly used PCMs, VO_2 and GST, suffer from high optical propagation losses even in their dielectric states. More recently, a new PCM, $\text{Ge}_2\text{Sb}_2\text{Se}_4\text{Te}_1$ (GSST) has been reported^{16,17}, which exhibits significantly low propagation loss at dielectric state compared to the traditional PCMs. An ultra-low extinction coefficient, $k = (1.8 \pm 1.2 \times 10^{-4})$ of the GSST at dielectric state was measured at the wavelength of 1550 nm¹⁷. Particularly, a large index-change of the GSST can be generated by the self-holding phase-transition between the amorphous (a-) and crystalline (c-) states, which can enable the nonvolatile capability to sustain the switches' states even in the absence of external powers. Therefore, a nonvolatile RMDS with a high performance would be achieved by utilizing the GSST-PCM.

In this paper, we propose and optimise a nonvolatile and ultra-low-loss RMDS via a triple-waveguide directional coupler (DC) with the GSST-PCM and a two-waveguide DC. An input quasi- TM_0 mode can be correspondingly converted to the quasi- TM_1 modes of two individual multimode waveguides (WGs) according to a- and c-states of the GSST-PCM, respectively. An ultra-compact footprint, ultra-low losses and high ERs of the proposed RMDS would be achieved benefiting from the GSST-PCM and triple-WG DC structure. The proposed RMDS is optimised by using the full-vectorial finite element method (FV-FEM) and 3D full-vectorial finite difference time domain method (3D-FV-FDTD).

Results

Schematic and Principle.

The schematic diagram of the proposed RMDS is shown in Fig. 1(a), consisting of a triple-WG DC and a two-WG DC. The triple-WG DC is comprised of an input SM-WG-1, a central WG-G with GSST, and an external bus WG-2. The input fundamental TM mode can be transferred into the bus WG-2 and outputs at port O_2 , when the state of the GSST is amorphous at “OFF” state of the RMDS. While the c-GSST is triggered at “ON” state, the input quasi- TM_0 mode would propagate along the input SM-WG-1 without mode coupling due to the phase-mismatching. Following this, the input quasi- TM_0 mode will be converted to the quasi- TM_1 mode in the bus WG-3 of the two-WG DC and output at port O_1 . It can be observed from Fig. 1(a) that the coupling lengths are denoted by L_{OFF} and L_{ON} for the triple- and two-WG DCs, respectively. The cross-sections of

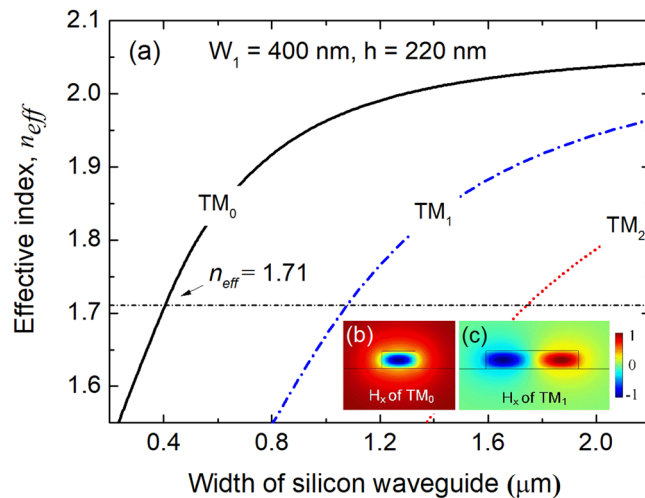


Figure 2. Phase-matching condition for isolated silicon waveguides. (a) Variations of the effective index with the width of the silicon waveguide; (b,c) are the H_x mode fields of the phase-matched quasi- TM_0 and quasi- TM_1 modes, respectively.

the triple- and two-WG DCs over the lengths of L_{OFF} and L_{ON} are shown in Fig. 1(b,c), respectively. The widths of the input SM-WG-1, central WG-G, bus WG-2 and -3 are represented by W_1 , W_G , W_2 and W_3 , respectively. The height of the silicon layer of these four WGs is denoted by h , which is chosen to be a common height, $h = 220$ nm of the silicon WG in this case. It can be observed from Fig. 1(b) that for the triple-WG DC, the separation in between each pair of three WGs is denoted by g_1 . The heights of the GSST and intermedium silica layers of the central WG-G are denoted by h_G and h_s , respectively. It can also be observed that for the two-WG DC, the separation between the input SM-WG-1 and the bus WG-3 is denoted by g_2 . In this case, the refractive indices of the silicon and silicon dioxide are taken as 3.47548 and 1.46, respectively at the operating wavelength of 1550 nm. A silica cladding is used to protect the silicon WGs. The refractive indices of the a- and c-GSST are taken as $3.39 + (1.8 \pm 1.2) \times 10^{-4}i$ and $5.14 + 0.42i$, respectively¹⁷.

The phase change of the GSST could be supposed to be similar to that of the GST-PCM¹⁸, which can be triggered via thermo-optic (TO), EO/electro-thermal (ET), and all-optical approaches¹⁹. In general, the a-GSST can be obtained by heating the c-GSST above the melting point followed by rapid cooling (< 1 ns). The c-GSST can be achieved by heating the a-GSST to be crystallized. By introducing a heater above the GSST, the phase state of the GSST can be simply adjusted based on the TO effect. An alternative TO approach could be the use of the pulsed laser to achieve the photo-thermal heating and then change the phase state²⁰. For the EO or ET based approach, the silicon sections can be doped as upper and lower contacts and then the applied voltage across the doped silicon can result in the desired thermal phase change via Joule heating current²¹. For the all-optical approach, a pump light can be used to go through the c-GSST section and be partly absorbed by c-GSST due to the relatively high absorption loss of c-GSST, which can also provide the desired thermal phase change for re-amorphization²². However, it may be difficult to achieve recrystallization due to the ultra-low extinction coefficient, $k = (1.8 \pm 1.2 \times 10^{-4})$ of a-GSST. In this case, the phase transition of the GSST is expected to be achieved by using the pulsed laser induced photo-thermal heating, which can be implemented without any electrode. In future, the approach based on the micro-heater or electro-thermal effect may be preferable for flexible photonic integrated circuits.

Characterization of mode properties. Firstly, the design of the triple-WG DC section with the GSST-PCM is studied by using the FV-FEM. The proposed triple-WG DC operates at two states: (a) for the “OFF” state with a-GSST, the input quasi- TM_0 mode is converted to the quasi- TM_1 mode of the bus WG-2 under the phase-matching condition; (b) for the “ON” state with c-GSST, the input quasi- TM_0 mode propagates along the input SM-WG-1 without any mode coupling. To achieve a maximum mode coupling efficiency at “OFF” state, the phase-matching condition for the input SM-WG-1, central WG-G with a-GSST and the bus WG-2 should be satisfied for the triple-WG DC. Variations of the effective index with the width of the silicon WG are shown in Fig. 2(a), in which the size of the input SM-WG-1 is taken as $W_1 \times h = 400 \text{ nm} \times 220 \text{ nm}$. The effective index of the quasi- TM_0 mode of the input SM-WG-1 is calculated to be $n_{\text{eff}} = 1.71$, denoted by a horizontally dash-dotted line in Fig. 2(a). The phase-matched width of the bus WG-2 is determined to be $W_2 = 1.075 \mu\text{m}$. The H_x mode fields of the phase-matched quasi- TM_0 and quasi- TM_1 modes are shown in Fig. 2(b,c), respectively.

For the triple-WG DC, more supermodes would be generated compared to the two-WG DC. In this case, the input quasi- TM_0 should be phase-matched with the quasi- TM_1 mode of the bus WG-2. Hence, three supermodes (TM-A, TM-B, and TM-C) are studied and the supermode fields are shown in Fig. 3. In the calculation, the parameters of the triple-WG DC are set as: $W_1 = 400$ nm, $W_2 = 1.075 \mu\text{m}$, $g_1 = 200$ nm, $h_G = 100$ nm and $h_s = 0$ nm. The E_y fields of the TM-A, TM-B, and TM-C supermodes are shown in Fig. 3(a-c), respectively. The Poynting vectors, $P_z(x, y)$ of these three supermodes are also calculated and shown in Fig. 3(d-f), respectively. To

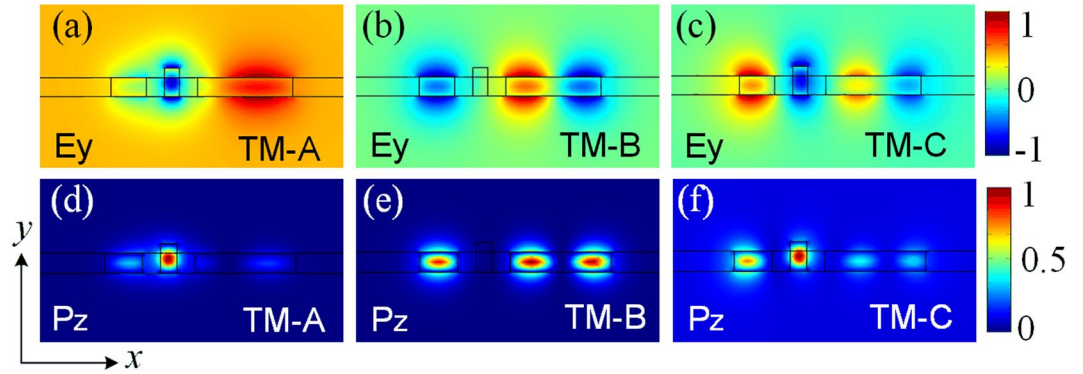


Figure 3. Supermode fields of the triple-waveguide directional coupler. (a–c) are the E_y fields of the TM-A, TM-B and TM-C supermodes, respectively; (d–f) are the $P_z(x, y)$ fields of the TM-A, TM-B and TM-C supermodes, respectively.

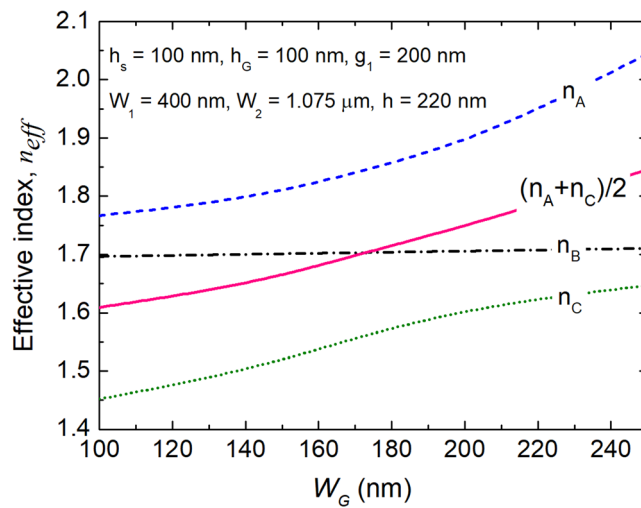


Figure 4. Phase-matching condition for the triple-WG DC. Variations of the effective index with the width of the central WG-G.

meet the phase-matching condition for this triple-WG DC, the effective indices of the TM-A, TM-B, and TM-C supermodes must satisfy the following condition²³:

$$n_A + n_C = 2n_B \tag{1}$$

where n_A , n_B , and n_C are the effective indices of the TM-A, TM-B, and TM-C supermodes, respectively.

Variations of the effective indices of n_A , n_B , n_C , and $(n_A + n_C)/2$ with the width of the central WG-G are shown in Fig. 4 and denoted by the dashed blue, dash-dotted black, dotted green and solid pink lines, respectively. The triple-WG DC with the parameters of $W_1 = 400$ nm, $W_2 = 1.075$ μm, $h = 220$ nm, $g_1 = 200$ nm, $h_G = 100$ nm and $h_s = 100$ nm is taken as an example. The effective indices of the n_A , n_C and $(n_A + n_C)/2$ are increased with the increase of W_G , while that of the n_B is kept constant due to the mode field of the TM-B supermode only confined in both the WG-1 and WG-2. According to Equation (1), the phase-matched W_G is chosen to be $W_G = 173$ nm.

Next, the coupling length of the triple-WG DC can be calculated by using the formula²³:

$$L_C = \frac{2\pi}{\beta_A - \beta_C} = \frac{\lambda_0}{2(n_A - n_B)} \tag{2}$$

where β_A and β_C are the propagation constants of the TM-A and TM-C supermodes, respectively; λ_0 is the operating wavelength. In order to achieve a compact RMDS, the coupling length should be optimised to be as short as possible. Variations of the coupling lengths with the heights of the intermedium silica and a-GSST layers are shown in Fig. 5(a,b), respectively. It can be noted from Fig. 5(a) that the coupling lengths for $h_G = 50$ nm, 100 nm and 150 nm are denoted by the solid black, dash-dotted red, and dotted blue lines, respectively. It can be noted from Fig. 5(a) that the coupling lengths are monotonically increased with the increase of h_s . Therefore, a minimum coupling length, L_{OFF} would be obtained in the absence of the intermedium silica layer of the central WG-G. It can also be noted from Fig. 5(a) that a shorter coupling length would be achieved with a larger height

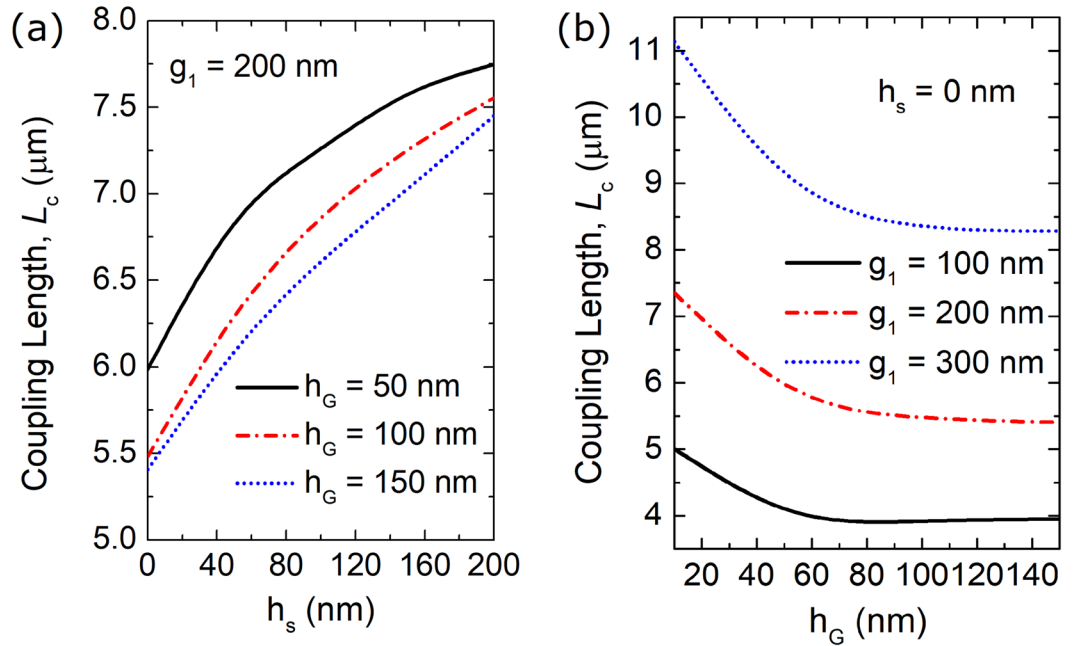


Figure 5. Variations of the coupling lengths with (a) height of the silica layer of the central WG and (b) height of the a-GSST layer, respectively. In the calculation, $W_1 = 400$ nm, $W_2 = 1.075$ μm , $h = 220$ nm; the phase-matched width of the central waveguide, W_G , should be changed accordingly to meet phase-matching condition.

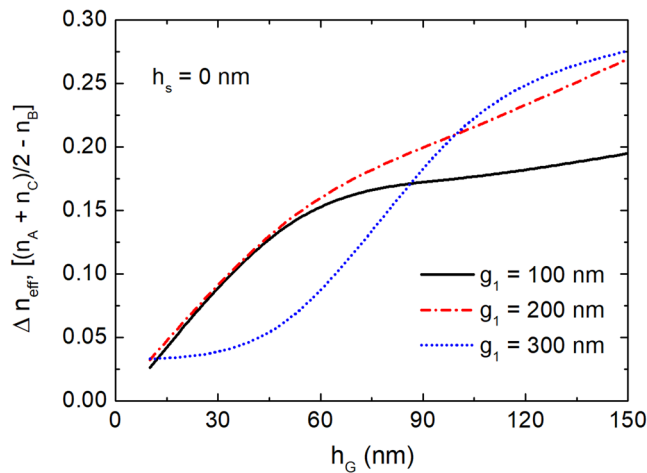


Figure 6. Variations of the difference of the effective index between $(n_A + n_C)/2$ and n_B with the height of the c-GSST layer.

of the a-GSST layer. It can be noted from Fig. 5(b) that the coupling lengths for $g_1 = 100$ nm, 200 nm and 300 nm are shown by the solid black, dash-dotted red, and dotted blue lines, respectively. A larger separation would induce a longer coupling length due to a weaker mode interaction. For a certain separation, the coupling length is decreased with the increase of the height of the GSST. Particularly, the coupling lengths go to the constants at $h_G = 50$ nm, 70 nm and 90 nm for $g_1 = 100$ nm, 200 nm and 300 nm, respectively.

The index difference, Δn_{eff} between $(n_A + n_C)/2$ and n_B at c-GSST state means the intensity of the phase-mismatch of the proposed triple-WG DC at “ON” state, which can determine the mode CT. Variations of the index difference with the height of the c-GSST layer are shown in Fig. 6 and denoted by the solid black, dash-dotted red and dotted blue lines for $g_1 = 100$ nm, 200 nm, and 300 nm, respectively. It can be noted that the index differences are increased with the increase of the height of the c-GSST layer, which can be explained by the fact that a larger index-modulation can be generated via a thicker c-GSST layer. If the index difference goes up to 0.15, the heights of the c-GSST layers need to be larger than 57.9 nm, 54.5 nm and 79.8 nm for $g_1 = 100$ nm, 200 nm and 300 nm, respectively. The corresponding coupling lengths are calculated to be $L_{\text{OFF}} = 4.0$ μm , 5.89 μm and 8.5 μm . Although a more compact coupling length can be obtained with a narrower separation, a higher

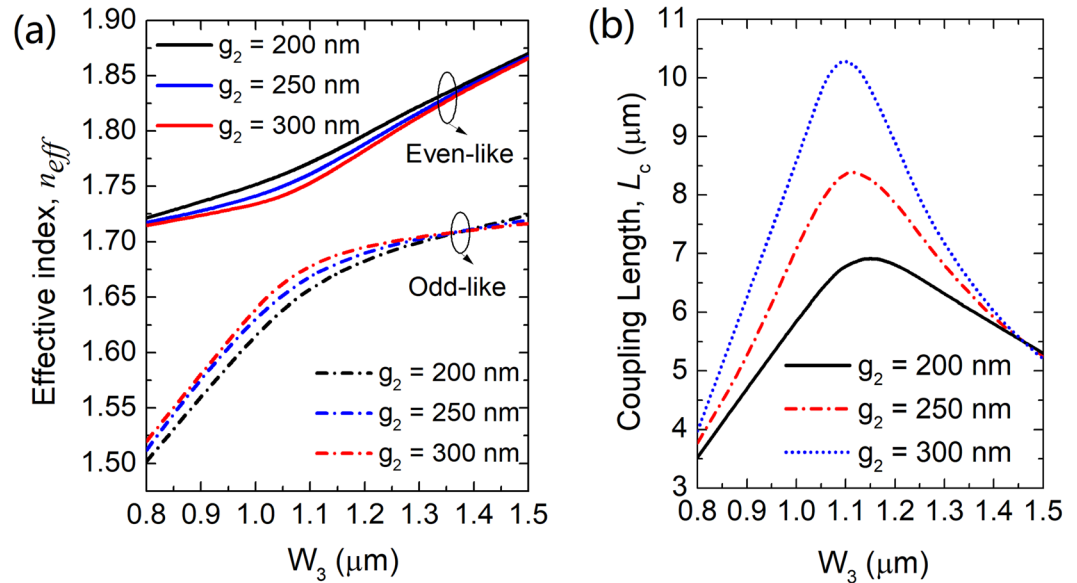


Figure 7. Variations of (a) effective index and (b) coupling length with the width of the bus WG-3, respectively for the two-WG DC.

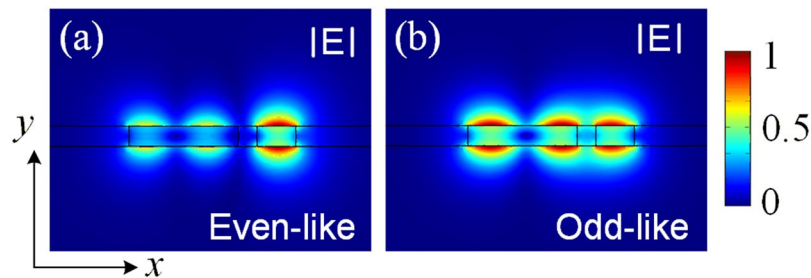


Figure 8. Supermode fields of the two-WG DC. E-field intensities of (a) even-like and (b) odd-like supermodes, respectively.

mode CT would be generated due to the stronger mode interaction. In order to balance the coupling length and the mode CT, the propagation characteristics of the proposed triple-WG DC will be studied by using the 3D-FV-FDTD in the following section.

For the “ON” state of the proposed RMDs, the input quasi-TM₀ mode would directly propagate along the input SM-WG-1 and then be coupled to the quasi-TM₁ mode of the bus WG-3 via a two-WG DC. Although the phase-matching condition between the isolated SM-WG-1 and bus WG-3 can be obtained from Fig. 2, it is essential to study that of the combined two-WG of the DC, which maybe dramatically different with each other due to the strong mode-interaction. Variations of the effective index with the width of the bus WG-3 are shown in Fig. 7(a). The even-like and odd-like supermodes are denoted by the solid and dash-dotted lines, respectively. The separations, $g_2 = 200$ nm, 250 nm and 300 nm are shown by the black, blue and red lines, respectively. It can be noted from Fig. 7(a) that the effective indices of the even-like and odd-like supermodes become closer near $W_3 = 1.1 \mu\text{m}$ and get mixed to form two phase-matched supermodes. The coupling length of the two-WG DC can be calculated based on the formula²⁴: $L_c = \pi / (\beta_{\text{even-like}} - \beta_{\text{odd-like}})$, where $\beta_{\text{even-like}}$ and $\beta_{\text{odd-like}}$ are the propagation constants of the even-like and odd-like supermodes, respectively. Variations of the coupling lengths of the two-WG DC with the width of the bus WG-3 are shown in Fig. 7(b). The coupling length is increased with the increase of the separation. Under the phase-matching conditions ($W_3 = 1.15 \mu\text{m}$, $1.11 \mu\text{m}$ and $1.1 \mu\text{m}$), the coupling lengths, L_{ON} are calculated to be $L_{\text{ON}} = 6.9 \mu\text{m}$, $8.4 \mu\text{m}$ and $10.3 \mu\text{m}$ for $g_2 = 200$ nm, 250 nm and 300 nm, respectively. The mode fields of two supermodes at $g_2 = 200$ nm are calculated by using the FV-FEM and shown in Fig. 8. The E-field intensities of the phase-matched even-like and odd-like supermodes are shown in Fig. 8(a,b), respectively. Similar to the triple-WG DC, a narrower separation of the two-WG DC would induce a higher mode CT. The balance between the coupling length and the mode CT will also be studied by using the 3D-FV-FDTD.

Operation and bandwidth. The propagation characteristics of the proposed RMDs are investigated by using the 3D-FV-FDTD. In order to evaluate the performance of the proposed RMDs, the insertion loss (IL) and mode ER are studied and calculated by using the formulas²³:

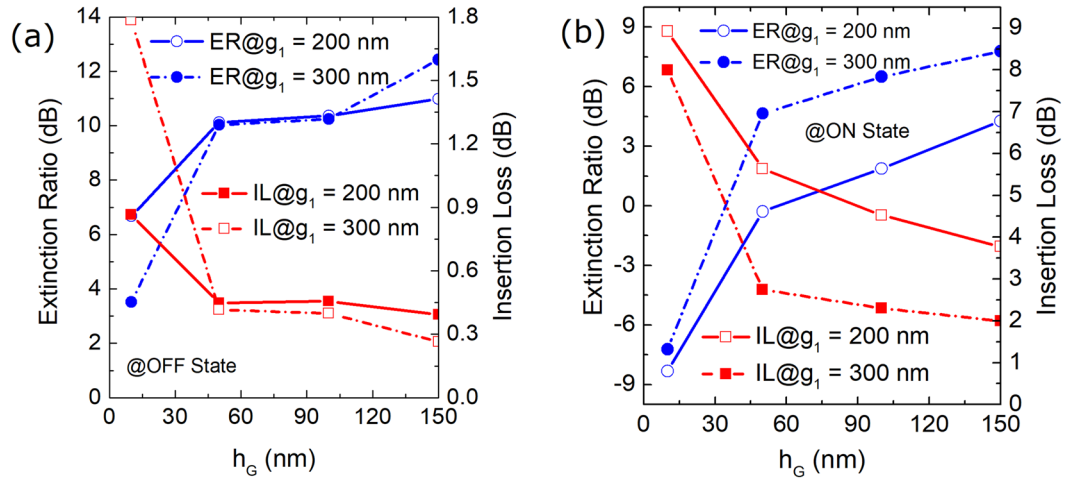


Figure 9. Variations the ER (left y-axis) and IL (right y-axis) with the height of the GSST layer for (a) OFF and (b) ON states, respectively for the triple-WG DC.

$$IL_{\text{OFF}} = -10\log_{10}\left(\frac{P_{O2}}{P_{I1}}\right) \tag{3}$$

$$IL_{\text{ON}} = -10\log_{10}\left(\frac{P_{O1}}{P_{I1}}\right) \tag{4}$$

$$ER_{\text{OFF}} = 10\log_{10}\left(\frac{P_{O2}}{P_{O1}}\right) \tag{5}$$

$$ER_{\text{ON}} = 10\log_{10}\left(\frac{P_{O1}}{P_{O2}}\right) \tag{6}$$

where P_{I1} is the input power at port I_1 ; P_{O1} and P_{O2} are the output powers at ports O_1 and O_2 , respectively. The mode CT of the proposed RMDS is calculated by $CT = -(IL + ER)$. For the triple-WG DC section, variations of the ER (left y-axis) and IL (right y-axis) with the height of the GSST layer are calculated based on the 3D-FV-FDTD and shown in Fig. 9(a,b) for the “OFF” and “ON” states, respectively. It can be noted from Fig. 9(a) that at “OFF” state, the ER is increased with the increase of h_G for both $g_1 = 200$ and 300 nm, while the IL is decreased. Similarly, it can be noted from Fig. 9(b) that the ER is increased and the IL is decreased with the increase of h_G for the “ON” state. Although a higher ER and a lower IL can be obtained with a larger h_G , it would induce a critical fabrication process for the central WG due to the large height-to-width ratio (H/W ratio). In this case, the height of the GSST layer of $h_G = 150$ nm is considered.

Variations of the ER (left y-axis) and IL (right y-axis) with the gap, g_1 are shown in Fig. 10(a). At both “OFF” and “ON” states, the ERs are monotonously increased as a function of the gap, g_1 . At “ON” state, the IL is dramatically decreased from 3.7 dB at $g_1 = 200$ nm to only 0.54 dB at $g_1 = 500$ nm. The IL at “OFF” state is < 0.4 dB in the whole range and goes to only 0.12 dB at $g_1 = 500$ nm, benefiting from the low-loss of the a-GSST-PCM. However, the absorption loss of the a-GSST [$k = (1.8 \pm 1.2) \times 10^{-4}$] should be taken into account, which is calculated by using the formula²⁵: $L_{\text{abs}} = 20\log_{10}[\exp(-\beta_{\text{im}}L_{\text{OFF}})]$, where β_{im} is the imaginary part of the propagation constant of the central WG-G. Variations of the coupling length (left y-axis) and absorption loss of central WG-G with a-GSST (right y-axis) as a function of the gap, g_1 is shown in Fig. 10(b). It can be noted that with the gap, g_1 changing from 200 nm to 500 nm, the coupling length, L_{OFF} is increased from $5.4 \mu\text{m}$ to $19.0 \mu\text{m}$ and then the absorption loss is slightly increased from 0.008 dB (2.1% of IL at “OFF” state) to 0.028 dB (23% of IL at “OFF” state), which is relatively and reasonably small compared to the total IL. Hence, the IL is decreased with the increase of the gap, g_1 , as stated in Fig. 10(a). In this case, an appropriate gap, $g_1 = 500$ nm is chosen to balance the ER/IL and L_{OFF} . The coupling length of the triple-WG DC is calculated to be $L_{\text{OFF}} = 19.0 \mu\text{m}$. The E_y fields along the propagation direction at “OFF” and “ON” states are shown in Fig. 10(c,d), respectively. It can be observed that at “OFF” state, the input optical power of the quasi-TM₀ mode is transferred to that of the quasi-TM₁ mode of the bus WG-2, while the input power propagates along the input SM-WG-1 without mode coupling at “ON” state.

As shown in Fig. 10(c), there is a weak coupling at “OFF” state between the SM-WG-1 and WG-2-O₂ even if the central WG-G with GSST is cut off. An s-shape bend waveguide could be added to gradually separate the SM-WG-1 and WG-2-O₂ to reduce unnecessary IL, which is shown in Fig. 11 as an inset. The length, L_s and offset of the s-shape bend waveguide are chosen to be $15.0 \mu\text{m}$ and $1.0 \mu\text{m}$, which can provide an enough separation

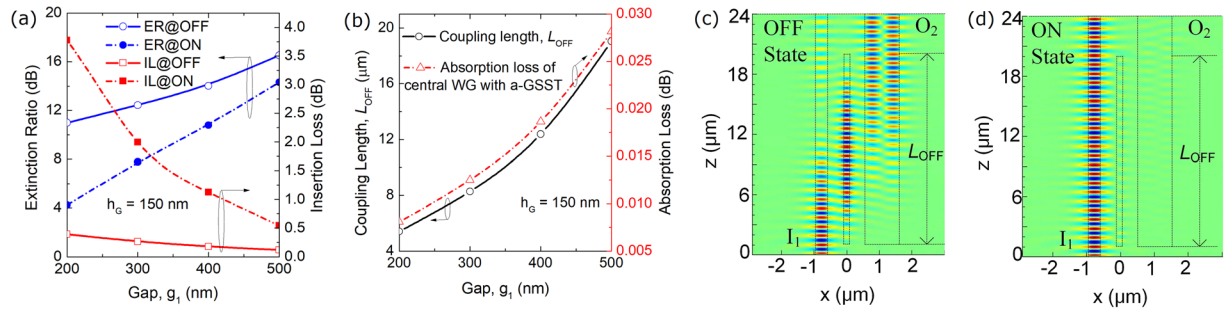


Figure 10. (a) Variations the ER (left y-axis) and IL (right y-axis) with the gap, g_1 ; (b) Variations of the coupling length (left y-axis) and absorption loss of central WG with amorphous-GSST (right y-axis) as a function of the gap, g_1 ; E_y fields along the propagation direction at (c) OFF and (d) ON states, respectively for the triple-WG DC.

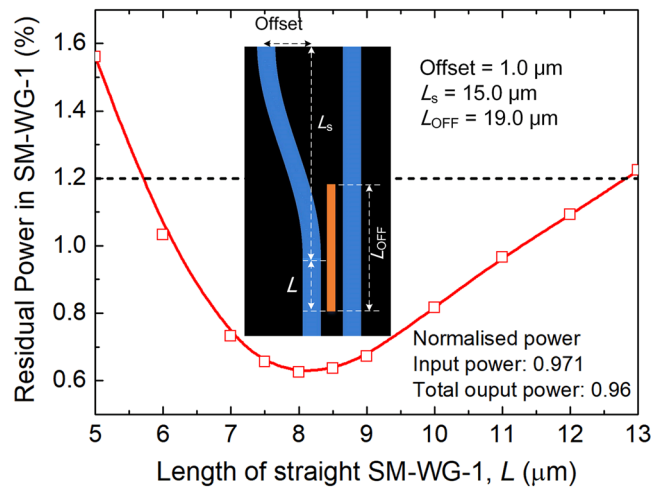


Figure 11. Variations of the normalised residual power in SM-WG-1 with the length of straight section of SM-WG-1, L . The inset is the schematic of triple-waveguide coupler with an s-shape bend waveguide.

between the SM-WG-1 and WG-2- O_2 . We calculated the normalised residual power in SM-WG-1 by varying the length of the straight section of SM-WG-1, L . The normalised residual power in SM-WG-1 without an s-shape bend waveguide is calculated to be 1.2%, as denoted by a horizontally dashed-black line in Fig. 11. It can be noted that by implementing an s-shape bend waveguide, the normalised residual power in SM-WG-1 is reduced from 1.2% to only 0.62% with an optimal $L = 8.0 \mu\text{m}$. The IL is slightly decreased from 0.1 dB to 0.078 dB and the mode CT is subsequently decreased from -19.08 dB to -21.9 dB.

Next, the propagation characteristics of the two-WG DC section are studied by using the 3D-FV-FDTD. Variations of the mode CT (left y-axis) and L_{ON} (right y-axis) with the gap, g_2 are shown in Fig. 12(a). It can be noted that the mode CT is decreased with the increase of the gap, g_2 , while the coupling length is increased. In this case, the gap, $g_2 = 300$ nm is selected with an acceptable coupling length of $L_{ON} = 10.3 \mu\text{m}$ and a low mode CT of -19.7 dB. The E_y field along the propagation direction is shown in Fig. 12(b), which shows that the input quasi- TM_0 mode is totally converted to the quasi- TM_1 mode of the bus WG-3.

Next, the performance of the optimised RMDS is investigated by utilizing the 3D-FV-FDTD. The optical fields along the propagation direction at “OFF” and “ON” states are shown in Fig. 13(a,b), respectively. At “OFF” state with a-GSST-PCM, the input quasi- TM_0 mode is switched to the first-order TM-mode of the bus WG-2 and outputs at port O_2 . While at “ON” state with c-GSST-PCM, the input quasi- TM_0 mode is switched to the quasi- TM_1 mode of the bus WG-3 and outputs at port O_1 . The ERs (ILs) are calculated to be 18.98 dB (0.10 dB) and 22.28 dB (0.58 dB) for the “OFF” and “ON” states, respectively. The CTs at “OFF” and “ON” states are -19.08 dB and -22.86 dB, respectively. The total coupling length of the optimised RMDS is $L_{OFF} + L_{ON} = 29.3 \mu\text{m}$, which is an ultra-compact size compared with that of the MZIs based ones (~several hundreds of micrometers)⁹. We need to pay attention to Fig. 13(b) that the output pattern at “ON” state has a certain oscillation, which indicates that the out-coupled field is actually composed of mixed modes. As the bus WG-3 with the optimised width of 1.1 μm , two TM modes (TM_0 and TM_1) and three TE modes (TE_0 , TE_1 , and TE_2) can be supported in this waveguide. The normalised power of the mixed modes in the bus WG-3 is calculated by using the mode expansion method, which shows that the out-coupled field of the bus WG-3 consists of both the TM_0 and TM_1 modes with 2.155% and 97.845% of total output power, respectively. The IL and mode ER at “ON” state would be slightly deteriorated to be 0.68 dB and 22.18 dB, respectively.

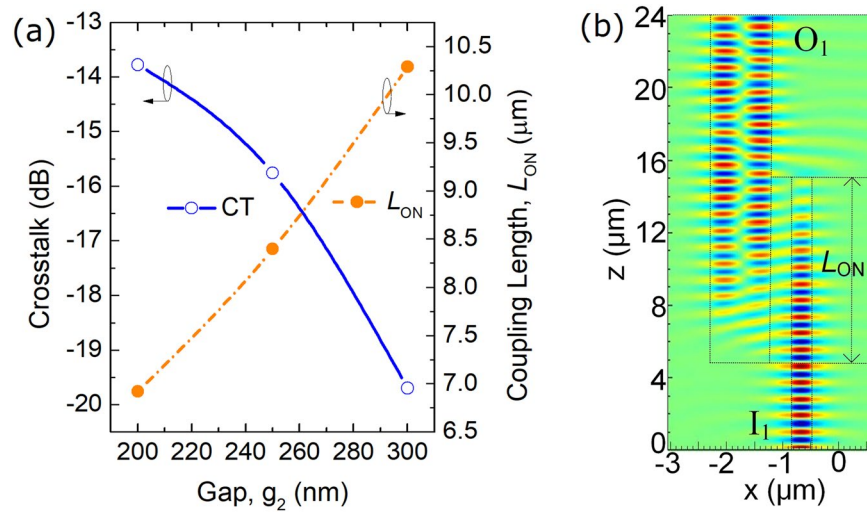


Figure 12. (a) Variations of the mode CT (left y-axis) and L_{ON} (right y-axis) with the gap, g_2 ; (b) E_y field along the propagation direction for the two-WG DC.

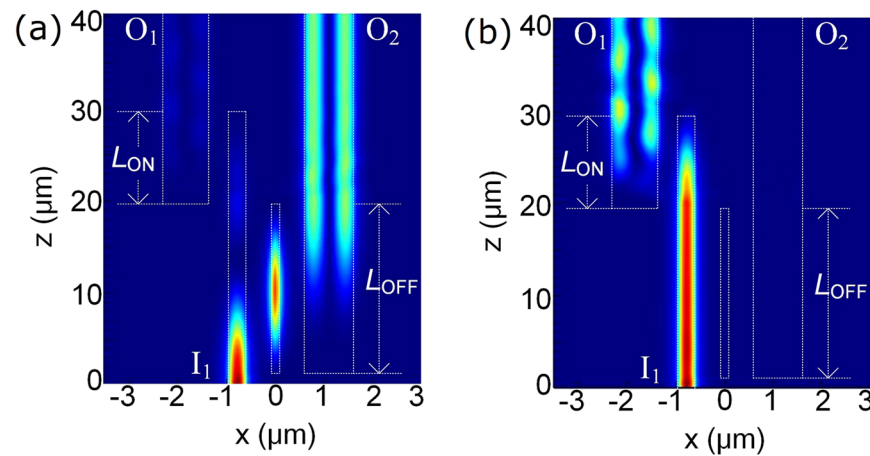


Figure 13. Optical fields along the propagation direction at (a) OFF and (b) ON states, respectively for the optimised RMDS.

The bandwidth of the RMDS is key to the on-chip MDM systems for constructing hybrid MDM-WDM networks. Variations of the power transmission with the operating wavelength of the optimised RMDS is shown in Fig. 14. It can be noted that the high ER of >17.3 dB can be achieved for both the states over 100 nm spectral bandwidth. The IL_{ON} is lower than 1.0 dB over 80 nm from 1520 nm to 1600 nm and the 1dB- IL_{OFF} bandwidth is over 60 nm from 1520 nm to 1580 nm. Compared to the MZIs based RMDS, the IL is significantly decreased from several dB to less than 1.0 dB⁹. Compared to the micro-rings based RMDS, the bandwidth is dramatically increased from a narrow bandwidth of only <13 GHz to 100 nm¹⁰. The proposed RMDS shows a high performance for providing an efficient approach to construct a hybrid MDM-WDM system.

As shown in Fig. 14, the ER at “OFF” state as a function of wavelength has a large fluctuation. The reason for this fluctuation at “OFF” state can be explained as two aspects: variations of the coupling length and the normalised power of mixed modes in bus WG-3 with the operating wavelength. In order to analyze the change of the coupling length with the operating wavelength, we define the ratio of the coupling length as: L_c ratio = $L_c / (L_c$ at 1550 nm). With the optimal parameters of $W_1 = 400$ nm, $W_2 = 1.075$ μm , $W_3 = 1.1$ μm , $W_p = 134.7$ nm, $g_1 = 500$ nm, and $g_2 = 300$ nm, variations of the ratio of the coupling length for both L_{OFF} and L_{ON} with the wavelength are shown in Fig. 15. It can be noted that both the L_{OFF} ratio and L_{ON} ratio are monotonously decreased with the increase of the operating wavelength in between 1500 nm and 1600 nm.

For the triple-WG DC over the bandwidth of 1500 nm \sim 1550 nm, the calculated coupling length would be larger than the physical length, L_{OFF} at 1550 nm of the central WG-G, which would induce a residual power remaining in the input SM-WG-1. In addition, a longer coupling length will be achieved for a smaller wavelength. Hence, for the bandwidth in between 1500 nm and 1550 nm, a larger deterioration of the mode ER was induced with a smaller wavelength, as shown in Fig. 14. For the triple-WG DC over the bandwidth of 1550 nm \sim 1600 nm, the calculated coupling length will be shorter than the physical length of the central WG-G. The input

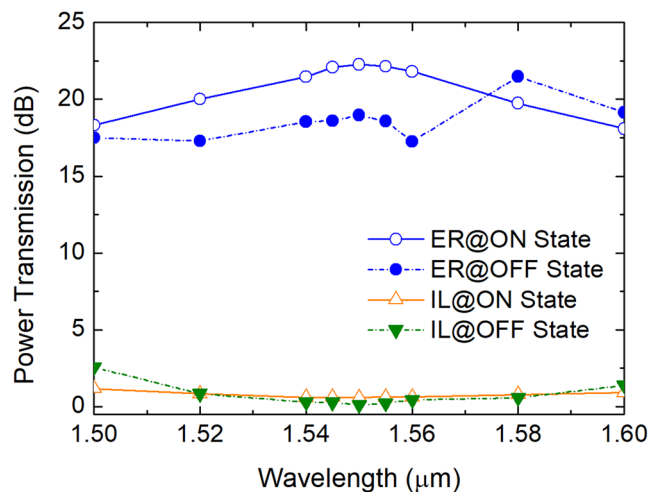


Figure 14. Variations of the power transmission with the operating wavelength of the optimised RMDS.

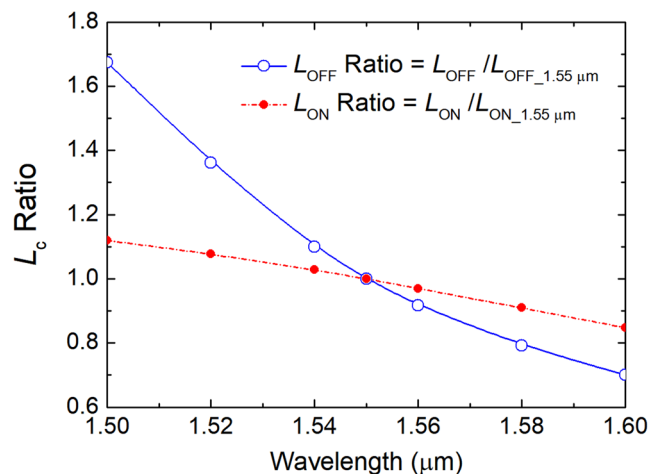


Figure 15. Variations of the ratio of coupling length, $[L_c / (L_c \text{ at } 1550 \text{ nm})]$ with the operating wavelength.

quasi- TM_0 mode will be firstly coupled to the quasi- TM_1 mode in the bus WG-2 and then be coupled back to the central WG-G, and then may be coupled back to the input SM-WG-1 depending on the calculated coupling length, which may also induce a residual power remaining in the input SM-WG-1. However, the mode ER at 1580 nm is larger than that at 1550 nm, as shown in Fig. 14. We checked the propagation field of the triple-WG DC at 1580 nm and found that the back-coupled field in the central WG-G radiates at the end of this waveguide and with only a tiny power (0.62%) coupled back to the input SM-WG-1. But, 1.7% and 0.884% of the total power is coupled back to the input SM-WG-1 for 1560 nm and 1600 nm, respectively. Therefore, a fluctuation is induced in between 1550 nm and 1600 nm, as shown in Fig. 14.

Next, variations of the normalised power of mixed modes in the bus WG-3 with the operating wavelength are calculated and shown in Fig. 16. It can be noted that for the two-WG DC, the power out-coupled to the quasi- TM_0 mode of the bus WG-3 is increased with the increase of the operating wavelength, whereas that out-coupled to the quasi- TM_1 mode is decreased. We should pay attention to the wavelength in between 1580 nm and 1600 nm, where a fluctuation of the normalised power of mixed modes is existed, subsequently further enlarges the variation of the mode ER at “OFF” state shown in Fig. 14.

Conclusion

In conclusion, we have proposed and optimised a nonvolatile and ultra-low-loss RMDS, consisting of a triple-WG DC with the GSST-PCM and a two-WG DC. Due to the self-holding phase-transition between a- and c-states of the GSST-PCM, the nonvolatile capability to sustain the switches’ states can be achieved to reduce the power-consumption. The proposed RMDS has been optimally designed by using the FV-FEM and 3D-FV-FDTD. The ultra-low insertion-losses of 0.10 dB and 0.68 dB of the optimised RMDS have been achieved for the “OFF” and “ON” states, respectively, benefiting from the low losses of the GSST-PCM at both a- and c-states. The mode CTs at “OFF” and “ON” states were -19.08 dB and -22.86 dB, respectively. The proposed RMDS was with a compact coupling length of $29.3 \mu\text{m}$ and high ERs of 18.98 dB and 22.18 dB for the “OFF” and “ON” states,

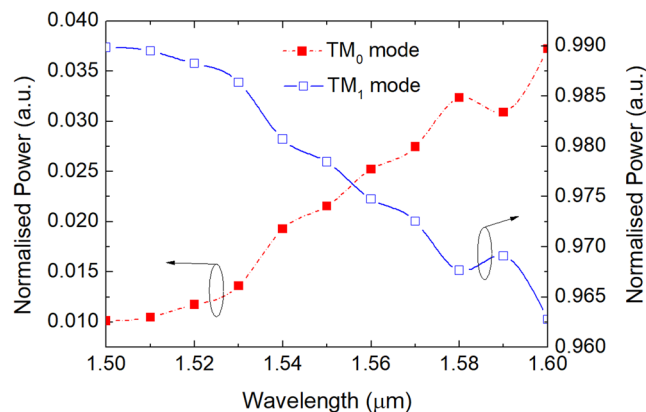


Figure 16. Variations of the normalised power of mixed mode in bus WG-3 versus wavelength.

respectively. A reasonable high ER of >17.3 dB has been achieved for both the states over 100 nm bandwidth, which offers the potential application in the S + C + L band MDM-WDM networks. The proposed RMDS can be applied in the MDM networks to provide a flexible mode routing and switching.

Methods

The mode characteristics of the isolated silicon waveguides and the combined triple-waveguide directional coupler (DC) are calculated by using the full-vectorial finite element method (FV-FEM). The refractive indices of the silicon, silicon dioxide, amorphous- and crystalline- $\text{Ge}_2\text{Sb}_2\text{Se}_4\text{Te}_1$ (GSST) are taken as 3.47548, 1.46, $3.39 + (1.8 \pm 1.2) \times 10^{-4}i$ and $5.14 + 0.42i$, respectively at the operating wavelength of 1550 nm. The phase-matching conditions for two-waveguide and triple-waveguide based DCs are determined by using the FV-FEM. The coupling lengths and the difference of the effective index are also optimized by using the FV-FEM. The propagation characteristics (propagation fields, mode crosstalk, insertion loss, and mode extinction ratio) of the optimised reconfigurable mode (De)MUX/switch (RMDS) are studied by using the 3D full-vectorial finite difference time domain (3D-FV-FDTD) method. The bandwidth of the optimised RMDS is also evaluated by using the 3D-FV-FDTD. The normalised power of the mixed mode in the bus waveguide-3 is investigated by using the mode expansion method (MEM).

References

- Zhang, Y., He, Y., Zhu, Q., Qiu, C. & Su, Y. On-chip silicon photonic 2×2 mode- and polarization-selective switch with low inter-modal crosstalk. *Photon. Res.* **5**, 521–526 (2017).
- Luo, L.-W. *et al.* WDM-compatible mode-division multiplexing on a silicon chip. *Nat. Commun.* **5**, 3069 (2014).
- Wang, J., Chen, P., Chen, S., Shi, Y. & Dai, D. Improved 8-channel silicon mode demultiplexer with grating polarizers. *Opt. Express* **22**, 12799–12807 (2014).
- Guan, X., Ding, Y. & Frandsen, L. H. Ultra-compact broadband higher order-mode pass filter fabricated in a silicon waveguide for multimode photonics. *Opt. Lett.* **40**, 3893–3896 (2015).
- Ye, M., Yu, Y., Sun, C. & Zhang, X. On-chip data exchange for mode division multiplexed signals. *Opt. Express* **24**, 528–535 (2016).
- Luo, Y., Yu, Y., Ye, M., Sun, C. & Zhang, X. Integrated dual-mode 3 dB power coupler based on tapered directional coupler. *Sci. Rep.* **6**, 23516 (2016).
- Zhou, T. *et al.* On-chip broadband silicon thermo-optic 2×2 four-mode optical switch for optical space and local mode switching. *Opt. Express* **26**, 8375–8384 (2018).
- Sun, C., Yu, Y., Chen, G. & Zhang, X. Integrated switchable mode exchange for reconfigurable mode-multiplexing optical networks. *Opt. Lett.* **41**, 3257–3260 (2016).
- Jia, H. *et al.* Optical switch compatible with wavelength division multiplexing and mode division multiplexing for photonic networks-on-chip. *Opt. Express* **25**, 20698–20707 (2017).
- Stern, B. *et al.* On-chip mode-division multiplexing switch. *Optica* **2**, 530–535 (2015).
- Xiong, Y., Priti, R. B. & Liboiron-Ladouceur, O. High-speed two-mode switch for mode-division multiplexing optical networks. *Optica* **4**, 1098–1102 (2017).
- Sun, S. *et al.* Hybrid photonic-plasmonic non-blocking broadband 5×5 router for optical networks. *IEEE Photon. J.* **10**, 4900312 (2017).
- Yang, L. *et al.* Proposal for a 2×2 optical switch based on graphene-silicon-waveguide microring. *IEEE Photon. Technol. Lett.* **26**, 235–238 (2014).
- Joushaghani, A. *et al.* Wavelength-size hybrid Si-VO₂ electroabsorption optical switches and photodetectors. *Opt. Express* **23**, 3657–3668 (2015).
- Liang, H. *et al.* Simulations of silicon-on-insulator channel-waveguide electro-optical 2×2 switches and 1×1 modulators using a $\text{Ge}_2\text{Sb}_2\text{Te}_3$ self-holding layer. *J. Lightw. Technol.* **33**, 1805–1813 (2015).
- Zhang, Y. *et al.* Broadband transparent optical phase change materials. In *Conference on Lasers and Electro-Optics, OSA Technical Digest* (Optical Society of America, JTh5C.4 2017).
- Zhang, Q. *et al.* Broadband nonvolatile photonic switching based on optical phase change materials: beyond the classical figure-of-merit. *Opt. Lett.* **43**, 94–97 (2018).
- Forouzmand, A. & Mosallaei, H. Dynamic beam control via Mie-resonance based phase-change metasurface: a theoretical investigation. *Opt. Express* **26**, 17948–17963 (2018).
- Haglund, R., Hewak, D., Ramanathan, S. & Hu, J. Feature issue introduction: Optical Phase Change Materials. *Opt. Mater. Express* **8**, 2967–2969 (2018).
- Zheng, J. *et al.* GST-on-silicon hybrid nanophotonic integrated circuits: a non-volatile quasi-continuously reprogrammable platform. *Opt. Mater. Express* **8**, 1551–1561 (2018).

21. Liang, H. *et al.* Simulations of silicon-on-insulator channel-waveguide electro-optical 2×2 switches and 1×1 modulators using a $\text{Ge}_2\text{Sb}_2\text{Te}_5$ self-holding layer. *J. Lightw. Technol.* **33**, 1805–1813 (2015).
22. Stegmaier, M., Rios, C., Bhaskaran, H. & Pernice, W. H. P. Thermo-optical effect in phase-change nanophotonics. *ACS Photonics* **3**, 828–835 (2016).
23. Ye, C., Liu, K., Soref, R. A. & Sorger, V. J. A compact plasmonic MOS-based 2×2 electro-optic switch. *Nanophotonics* **4**, 261–268 (2015).
24. Jiang, W., Kohli, N., Sun, X. & Rahman, B. M. A. Multi-poly-silicon-layer based spot-size converter for efficient coupling between silicon waveguide and standard single-mode fiber. *IEEE Photon. J.* **8**, 6600612 (2016).
25. Jiang, W. & Sun, X. TE-pass polarizer with cylinder array inserted in buffer layer of silica-on-silicon waveguide. *IEEE Photon. Technol. Lett.* **26**, 937–940 (2014).

Acknowledgements

This work was supported by the National Natural Science Foundation of China (NSFC) (Grant No. 61574080, 61274121, and 11704199), Natural Science Foundation of Jiangsu Province (Grant No. BK20180743), NUPTSF (Grant No. NY218108) and the Research Center of Optical Communications Engineering & Technology, Jiangsu Province. The author would like to thank Prof. B. M. Azizur Rahman at City, University of London for the insightful discussion, constructive comments, and rigorous numerical algorithm.

Author Contributions

W.F.J. gave the idea and carried out all the simulation work. W.F.J. prepared all the figures and wrote up the manuscript text.

Additional Information

Competing Interests: The author declares no competing interests.

Publisher's note: Springer Nature remains neutral with regard to jurisdictional claims in published maps and institutional affiliations.



Open Access This article is licensed under a Creative Commons Attribution 4.0 International License, which permits use, sharing, adaptation, distribution and reproduction in any medium or format, as long as you give appropriate credit to the original author(s) and the source, provide a link to the Creative Commons license, and indicate if changes were made. The images or other third party material in this article are included in the article's Creative Commons license, unless indicated otherwise in a credit line to the material. If material is not included in the article's Creative Commons license and your intended use is not permitted by statutory regulation or exceeds the permitted use, you will need to obtain permission directly from the copyright holder. To view a copy of this license, visit <http://creativecommons.org/licenses/by/4.0/>.

© The Author(s) 2018